The Astrophysical Journal, 823:126 (14pp), 2016 June 1 doi:10.3847/0004-637X/823/2/126

THERMAL CHARACTERISTICS AND THE DIFFERENTIAL EMISSION MEASURE DISTRIBUTION DURING A B8.3 FLARE ON 2009 JULY 4

Arun Kumar Awasthi[1], Barbara Sylwester[2], Janusz Sylwester[2], and Rajmal Jain[3]
[1] Astronomical Institute, University of Wroclaw, Wroclaw, Poland; arun.awasthi.87@gmail.com, awasthi@astro.uni.wroc.pl
[2] Solar Physics Division, Space Research Centre, Polish Academy of Sciences, Wroclaw, Poland
[3] Kadi Sarva Vishwavidyalaya, Gandhinagar, Gujarat, India
Received 2015 December 18; accepted 2016 April 6; published 2016 May 31

ABSTRACT

We investigate the evolution of the differential emission measure distribution (DEM[*T*]) in various phases of a B8.3 flare which occurred on 2009 July 04. We analyze the soft X-ray (SXR) emission in the 1.6–8.0 keV range, recorded collectively by the Solar Photometer in X-rays (SphinX; Polish) and the Solar X-ray Spectrometer (Indian) instruments. We conduct a comparative investigation of the best-fit DEM[*T*] distributions derived by employing various inversion schemes, namely, single Gaussian, power-law functions and a Withbroe–Sylwester (W–S) maximum likelihood algorithm. In addition, the SXR spectrum in three different energy bands, that is, 1.6–5.0 keV (low), 5.0–8.0 keV (high), and 1.6–8.0 keV (combined), is analyzed to determine the dependence of the best-fit DEM[*T*] distribution on the selection of the energy interval. The evolution of the DEM[*T*] distribution, derived using a W–S algorithm, reveals multi-thermal plasma during the rise to the maximum phase of the flare, and isothermal plasma in the post-maximum phase of the flare. The thermal energy content is estimated by considering the flare plasma to be (1) isothermal and (2) multi-thermal in nature. We find that the energy content during the flare, estimated using the multi-thermal approach, is in good agreement with that derived using the isothermal assumption, except during the flare maximum. Furthermore, the (multi-) thermal energy estimated while employing the low-energy band of the SXR spectrum results in higher values than that derived from the combined energy band. On the contrary, the analysis of the high-energy band of the SXR spectrum leads to lower thermal energy than that estimated from the combined energy band.

Key words: plasmas – radiation mechanisms: thermal – Sun: corona – Sun: flares – Sun: X-rays, gamma rays – techniques: spectroscopic

1. INTRODUCTION

Solar flares are some of the most energetic phenomena occurring in the atmosphere of our Sun, typically releasing 10^{27}–10^{32} erg of energy in $\sim 10^3$ s. This immense energy release is understood to be powered by magnetic energy via the process of magnetic reconnection (Shibata 1999; Jain et al. 2011a; Choudhary et al. 2013; Aschwanden et al. 2014; Dalmasse et al. 2015). A typical M-class solar flare can be observed across almost the entire electromagnetic spectrum (Benz 2008; Fletcher et al. 2011). Therefore, various energy release processes occurring at various heights in the solar atmosphere can be probed by the investigation of the observed multi-wavelength flare emission.

X-ray emission during solar flares mainly originates from the corona and upper chromosphere. Moreover, the X-ray emission recorded during a flare can serve as the best probe for studying various thermal and non-thermal plasma processes (Li et al. 2005; Saint-Hilaire & Benz 2005; Jain et al. 2008; Awasthi et al. 2014). Low-energy X-ray emission (<10 keV), also known as soft X-ray (SXR) emission, is understood to originate in the process of free–free, free-bound, and bound-bound emission due to the collision of charged particles (mostly electrons) with a thermal (Maxwell–Boltzmann) distribution. On the other hand, high-energy X-ray emission (hard X-rays) is known to be produced as a consequence of the thick-target bremsstrahlung of a non-thermal electron beam with the dense plasma in the chromosphere (Brown 1971; Kulinová et al. 2011). Moreover, SXR emission during a flare is understood to be produced by multi-thermal plasma (Aschwanden 2007; Jain et al. 2011b; Sylwester et al. 2014; Aschwanden et al. 2015b).

The study of the thermal characteristics of the flare plasma is performed through the inversion of the observed X-ray spectrum by postulating an empirical functional form of the differential emission measure (EM) distribution (DEM[*T*]). Although DEM [*T*] plays a key role in deriving the thermal characteristics, and in turn the energetics of the flare plasma, it is less accurately known due to the fact that the inversion of the observed radiation needs to be performed, which is a very ill-posed problem (Craig & Brown 1976). Moreover, several DEM[*T*] schemes which postulate a certain functional dependence of DEM on T, namely, single Gaussian, bi-Gaussian, power-law, etc., have been proposed (see Aschwanden et al. 2015b for exhaustive list of schemes). Furthermore, a Withbroe–Sylwester (W–S) maximum likelihood DEM inversion algorithm has been established by Sylwester et al. (1980) where the functional form of DEM[*T*] is not defined a priori. In this regard, a comparative survey of the aforementioned DEM schemes in the form of the derived thermal characteristics of the flare plasma is very necessary provided that the application of various inversion schemes results in similar outcomes. In addition, an inevitable restriction when deriving the complete thermal characteristics of the flare plasma is the availability of observations from different instruments in certain specific energy bands. Thermal emission can be best studied by measuring the X-ray spectrum in typically the 1–12 keV energy band. Observations in this energy band with high spectral and temporal cadence are very difficult to achieve from a single instrument due to the huge difference in flux during a flare across the energy band.

Therefore, we examine the temperature dependence of the DEM from the analysis of multi-instrument data for a B8.3

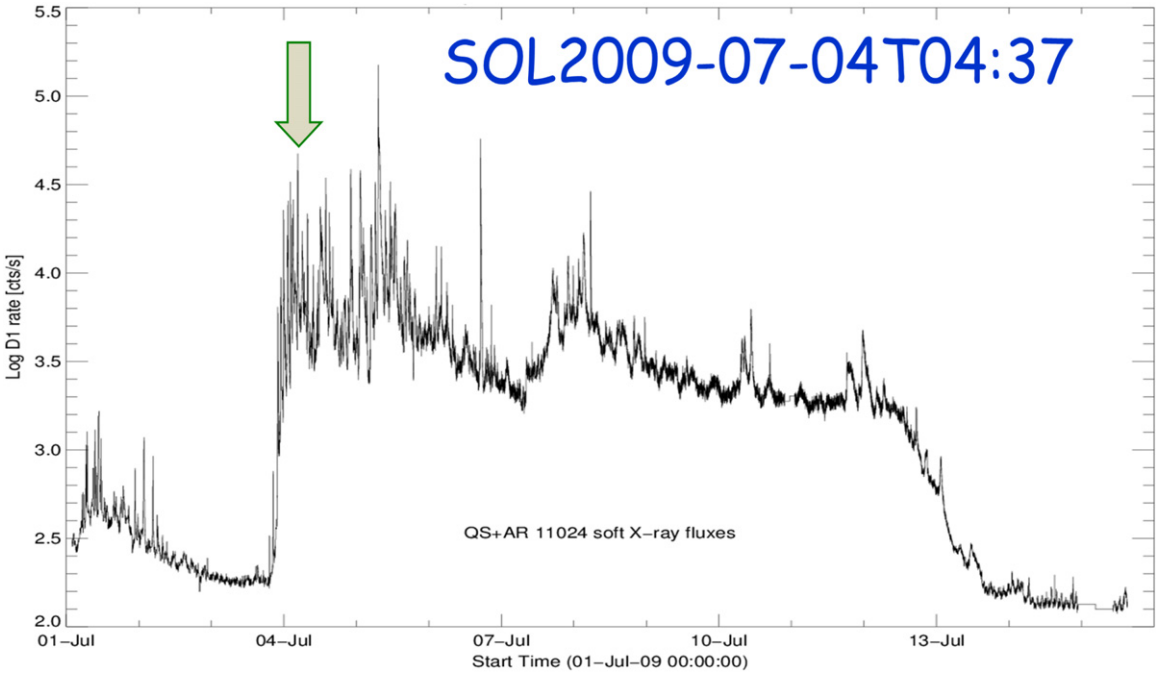

Figure 1. X-ray light curve of the solar corona, dominated by the emission from the single active region AR11024 with the flaring emission on top as seen by SphinX. Flare SOL2009-07-04T04:37, selected for the present study, is shown by an arrow.

flare which occurred on 2009 July 04. As the flare selected for the analysis is the only common event between Solar Photometer in X-rays (SphinX; a Polish instrument) and the Solar X-ray spectrometer (SOXS; an Indian instrument), the combined data set provides a unique opportunity for exhaustive study of the complete thermal characteristics of a small flare. Both of the instruments make use of Si PIN detectors for observing the solar atmosphere in the X-ray waveband. Section 2 presents the observations used for the present study along with the specifications of the respective instruments. In Section 3, we present the study of the DEM[T] distribution derived by employing different inversion schemes and its dependence on the selection of the energy band of the input SXR spectrum. In Section 4, the thermal energetics of the flare, estimated from the parameters derived from various schemes, are presented. Section 5 is comprised of the summary and conclusions.

2. OBSERVATIONS

We investigate a B8.3 intensity class flare which occurred on 2009 July 04 in active region AR11024. AR11024 appeared on the disk on 2009 July 3 and rotated off the disk on 2009 July 15. More than 500 flares or small brightenings have been observed by the SphinX mission for the SXR light curve during that time. Figure 1 shows the temporal evolution of the X-ray emission recorded by SphinX during this period.

The SOL2009-07-04T04:37 flare, selected for the present study, is the only event observed by both the SphinX and SOXS missions because SOXS usually observed the Sun in X-rays for only 2–3 hr a day. We analyze the X-ray spectra in the 1.6–5.0 keV and 5.0–8.0 keV energy bands, recorded from the SphinX and SOXS missions, respectively. We briefly discuss the data and the respective instruments' specifications as follows.

2.1. SphinX Mission

We analyze X-ray spectra in the 1.6–5.0 keV band (hereafter low-energy band) from the SphinX instrument (Gburek et al. 2011, 2013; Sylwester et al. 2012). SphinX, a spectrophotometer designed to observe the solar corona in SXRs, was flown on board the Russian *CORONAS-PHOTON* satellite on 2009 January 30. SphinX employed three Si PIN diode detectors to record X-rays in the energy range ~1.2–15.0 keV. The temporal and spectral cadence of the SphinX observations are as good as 6 μs and 0.4 keV, respectively. Detailed information regarding the observations, the procedure for calibration, and the data warehouse may be obtained from Gburek et al. (2013) and from the SphinX instrument homepage.[4]

2.2. SOXS Mission

X-ray spectra in the 5.0–8.0 keV band (hereafter high-energy band) during the flare were obtained by the SOXS instrument (Jain et al. 2005, 2008). SOXS employed two semiconductor devices, namely, a silicon (Si) PIN detector for recording X-ray observations in the energy range 4–25 keV and a Cadmium Zinc Telluride (CZT) detector for that in the energy range 4–56 keV. The energy resolution of the Si detector is ~0.8 keV while that for CZT detector is ~1.7 keV. The temporal cadence of the observations obtained from both detectors is 3 s during the quiet and gradual phase of the flare. However, an on board automated algorithm allowed the observations to be recorded with a 100 ms cadence during the rise to the peak phase of the flare. The data obtained during the entire observing period (2003 May–2011 April) of the SOXS mission and the analysis procedures are available on the instrument homepage.[5] In the present study, we employ the observations obtained from the Si

[4] http://156.17.94.1/sphinx_l1_catalogue/SphinX_cat_main.html
[5] https://www.prl.res.in/~soxs-data/

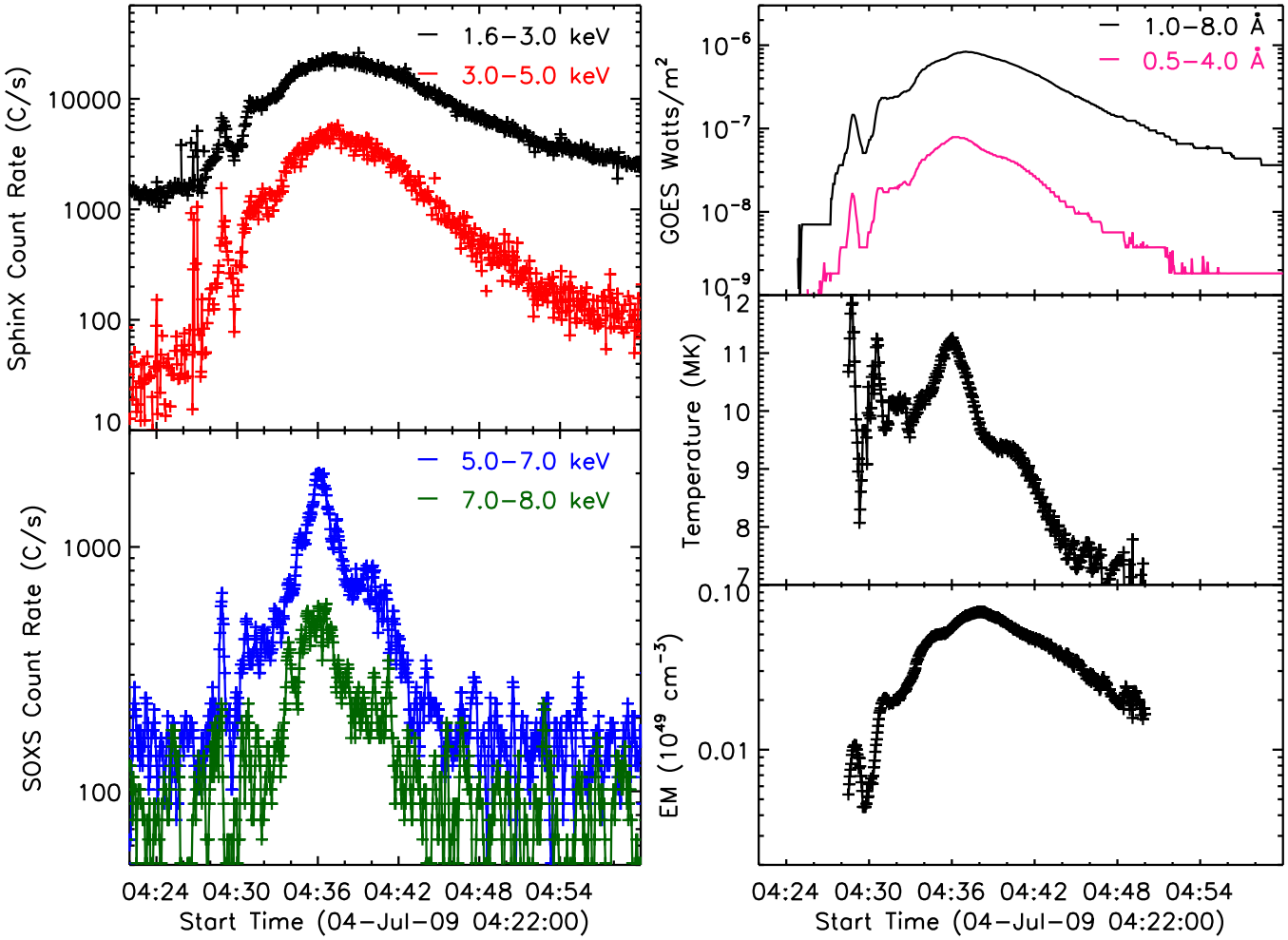

Figure 2. Left panel: temporal evolution of the X-ray count rate in 1.6–3.0 keV and 3.0–5.0 keV obtained from SphinX (top row) and that in 5.0–7.0 keV and 7.0–8.0 keV as recorded by SOXS (bottom row). Right panel: *GOES* flux in 1.0–8.0 Å and 0.5–4.0 Å (top row), temperature (middle row), and emission measure (bottom row).

detector because it has better energy resolution and sensitivity compared to the CZT detector.

The left panel of Figure 2 presents the evolution of the X-ray emission as observed by the SphinX (top row) and SOXS (bottom row) missions during the flare in various energy bands plotted with different colors. The intensity curves shown in black and red represent the X-ray emission recorded by SphinX in 1.6–3.0 keV and 3.0–5.0 keV, respectively. Furthermore, X-ray emission in 5.0–7.0 keV and 7.0–8.0 keV, drawn in blue and green, respectively, are obtained from SOXS.

It may be noted from the Figure 2 that SOXS receives higher background than that seen by SphinX. On the contrary, a comparison of the count rates recorded by SphinX and SOXS in the 4–6 keV range, that is, the energy band commonly covered by both instruments, revealed that SOXS observations are lower by a factor of ∼2.5. This may be attributed to the systematic difference of the sensitivities between the two instruments. Mrozek et al. (2012) reported higher flux in the SphinX 3–8 keV energy band compared to the observations obtained in the same energy range from the *RHESSI* mission by a factor varying in the range 2–6 keV. On the other hand, a comparison of the SOXS and *RHESSI* observations in the 6–12 keV energy band was performed by Caspi & Lin (2010) which resulted in the agreement of the spectra obtained from both instruments within 5%–10%. In this study, we prepared combined data by applying the previously noted "empirical normalization factor" in the records obtained from SOXS. On the other hand, we consider the flux recorded by SphinX to be the true flux because this is the only instrument available to observe X-ray emission at energies less than 4 keV during the flare. Therefore, the difference in inter-instrument sensitivity, and hence normalization factor, in this energy range cannot be established. However, in order to study the effect of this approximation, we have also carried out an investigation of the DEM distribution by applying the inverse normalization factor to the SphinX records while retaining the original SOXS counts. We discuss the effect of both of the noted cases on the thermal energy estimates as presented in Section 4.

2.3. Geostationary Operational Environmental Satellite (GOES)

GOES refers to a series of satellites dedicated to observing X-ray emission from the Sun as a star in two wavelength bands, namely, 1.0–8.0 Å and 0.5–4.0 Å. The right column of Figure 2 shows the background subtracted flux in the 1.0–8.0 Å and 0.5–4.0 Å bands plotted in black and red, respectively. We treat the observations averaged during 04:20–04:25 UT as background. The temperature and EM estimated from the flux-ratio

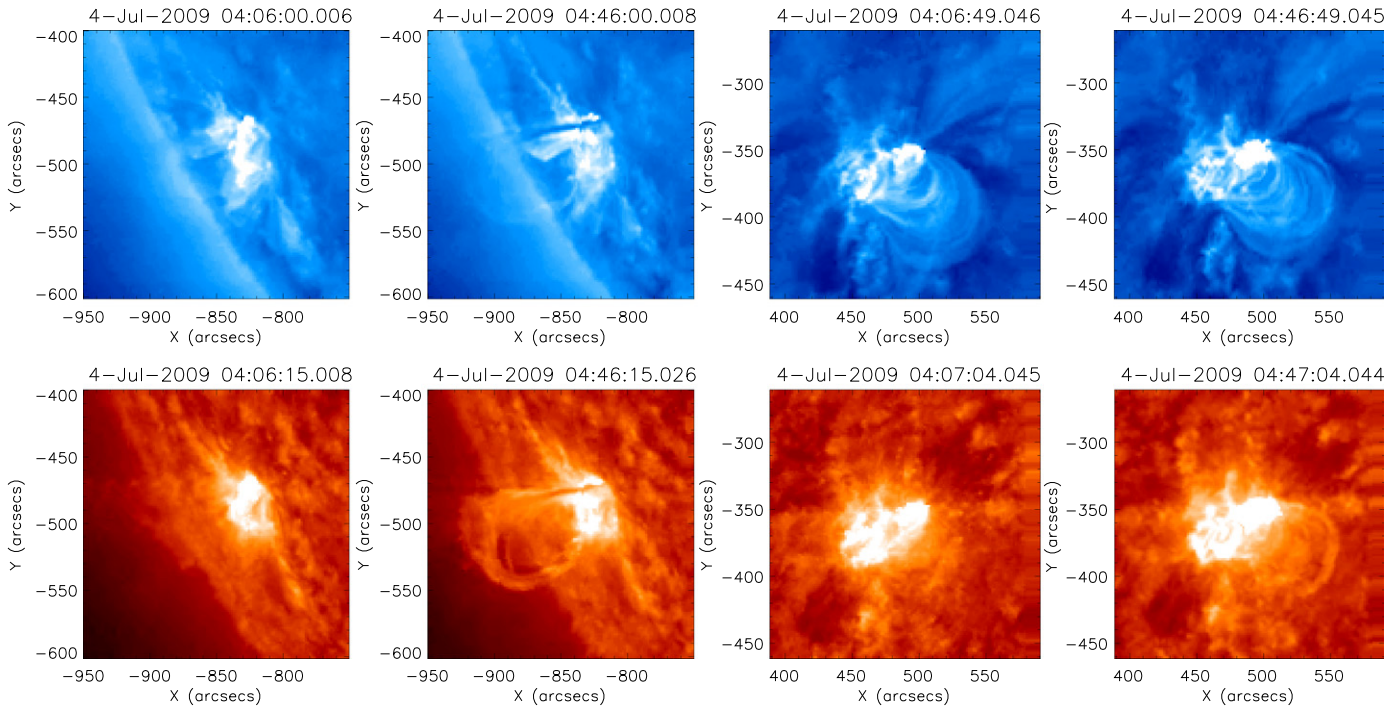

Figure 3. Time sequences of images in 171 Å (top row) and 304 Å (bottom row) obtained by the *STEREO* twin satellites during the flare. The images in the first two columns correspond to the side view of the flare obtained from *STEREO-A*, while those in the other two columns present the line-of-sight view of the flare as seen from *STEREO-B*.

technique adopted for *GOES* data are also plotted in the middle and bottom rows of the right panel in Figure 2, respectively. It may be noted that the temperature is found to vary in the range 7–12 MK while the EM varies in the range (0.003–0.08) $\times$ 10^{49} cm^{-3}. We use these T and EM estimates to calculate the thermal energy during the flare (see Section 4).

2.4. Morphology of the Flare in Extreme Ultraviolet (EUV) Emission

The temporal and morphological evolution of the flaring region is studied using observations obtained from the EUV Imaging Telescope (EIT; Delaboudinière et al. 1995) on board the *Solar and Heliospheric Observatory (SOHO)*. Moreover, images in the 171, 284, and 304 Å wavelengths, recorded by the *STEREO* twin satellites, are also processed. In Figure 3, we present the morphological evolution of the flaring region in 171 and 304 Å during the flare as obtained from *STEREO-A* and *B*.

From the time sequence of the EUV images presented in Figure 3, we note that although the flare event considered is a small B8.3 intensity class flare, it is associated with an eruption. The study of the eruption is outside of the scope of this paper. We estimate the volume of the emitting region from the EUV images to derive the thermal energetics of the flare as presented in Section 4.

3. DEM[*T*] DISTRIBUTION FROM THE APPLICATION OF VARIOUS INVERSION SCHEMES

In order to study the thermal characteristics of the flare plasma, we conduct an exhaustive investigation of the evolution of the DEM[*T*] relationship employing the X-ray spectra observed from SphinX and SOXS. We explore the dependence of the DEM[*T*] distribution, which is derived by employing various inversion schemes to the SXR spectra in various energy bands, namely, 1.6–5.0 keV (low energy), 5.0–8.0 keV (high energy), and 1.6–8.0 keV (hereafter combined energy). This study aims to understand the dependence of the best-fit DEM[*T*] representing a selective part of the SXR emission, which in turn presents the consequence of the restrictions posed by the co-temporal observations recorded in separate energy bands from different instruments, namely, SphinX and SOXS. In this study, we employ DEM inversion schemes which postulate the (1) single Gaussian and (2) power-law functional relationship of DEM to T. In addition, we also employ (3) a well-established W–S maximum likelihood inversion algorithm which is independent of a priori assumption of a functional form of DEM[*T*]. In the following, we present the thermal characteristics of X-ray emission during the flare as derived by applying the inversion schemes noted above.

3.1. DEM Varying as a Single-Gaussian Function over Temperature

We investigate the best-fit DEM[*T*] distributions, which were obtained by employing the scheme of single Gaussian functional dependence of DEM on *T*, on the observed SXR spectrum in the low-, high-, and combined-energy bands. However, first, we also employ this DEM scheme to a synthesized model multi-thermal spectrum. Below, we discuss the two previously mentioned cases.

3.1.1. DEM[T] Distribution of a Synthesized Model Multi-thermal Spectrum

We synthesize multi-thermal photon spectra using the model photon flux arrays corresponding to the isothermal plasma in the temperature range 1–23 MK with a temperature bin of log T = 0.1 MK. The isothermal photon spectrum at specific

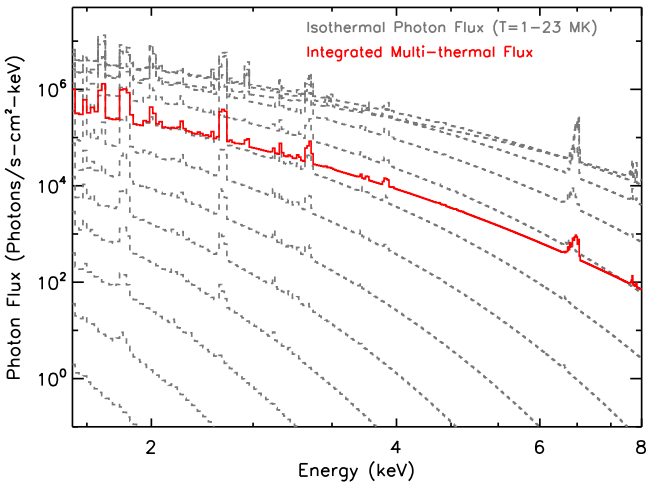

Figure 4. Spectra plotted in gray (dotted) represent the isothermal photon flux corresponding to the temperature range 1–23 MK with an interval of $\log T = 0.1$ MK. The plot drawn in red represents the integrated (multi-thermal) photon flux.

temperature and EM is calculated using the isothermal model (f_vth.pro) available in the SPectral EXecutive package within *Solar Soft Ware*. We derive EM values corresponding to a temperature from the EM model of Dere & Cook (1979), which is also available in the CHIANTI atomic database (Landi et al. 2012; Del Zanna et al. 2015). In addition, we consider the abundance to be 0.1 times the coronal abundance available in the CHIANTI distribution. Next, the multi-thermal photon spectrum is derived by the weighted sum of the isothermal spectra in following manner:

$$F_{\rm MT} = \sum_{k=T_{\rm min}}^{T_{\rm max}} w_k F(T_k, EM_k). \quad (1)$$

Here, $F(T_k, EM_k)$ is the isothermal photon flux and is shown by the gray (dotted) plots in Figure 4, while the multi-thermal flux ($F_{\rm MT}$) synthesized in this manner is over-plotted in red. Furthermore, w_k is the weight factor which is assumed to be a normalized Gaussian function of temperature with maximum at $T = 5.6$ MK and FWHM of ~5 MK, as shown in panel (d) of Figure 5. Such integration allows for a more realistic scheme of synthesizing the theoretical multi-thermal spectra compared to that adopted in Aschwanden (2007) and Jain et al. (2011b). They use a direct sum of the isothermal fluxes with equal weight, in which the synthesized multi-thermal photon spectrum is dominated by the contribution from the isothermal spectrum corresponding to the peak temperature.

Next, we forward fit the synthesized multi-thermal spectrum using DEM varying as a single Gaussian function of T. The form of the DEM[T] is considered as

$$\mathrm{DEM}[T] \propto \exp\left(\frac{-(\log T_{\rm p} - \log T)^2}{2\sigma^2}\right), \quad (2)$$

where $T_{\rm p}$ is the temperature at the peak of DEM [T] while σ is the Gaussian width. By iteratively varying the independent variables of Equation (2), namely, $T_{\rm p}$, σ, etc., a photon flux best-fit to the input synthesized multi-thermal photon spectra is derived. It is to be noted that the minimum and maximum temperature values for deriving the DEM[T] are fixed to 0.087 keV (1 MK) and 8.5 keV (100 MK), respectively. The best fit is assessed by estimating the reduced χ^2 in each step of the iteration, which converges to a small value. Following this procedure, we derive the best-fit parameters for the synthesized multi-thermal photon spectrum in the low- and high-energy bands. Next, we apply a similar procedure to derive the best-fit parameters for the input photon spectrum in the combined energy band. Panels (a), (b), and (c) of Figure 5 show the synthesized input multi-thermal photon spectrum (gray) overlaid by the best-fit model flux drawn in black, blue, and red for the low-, high-, and combined-energy bands, respectively. In addition, normalized residuals are also plotted in the respective panels. Moreover, panel (d) presents the DEM evolution corresponding to the best-fit model photon spectra.

Based on the aforementioned analysis presented in Figure 5, we find that the best-fit flux derived for the input photon spectrum in the low-energy band (panel (a)) does not provide a good fit (overestimation) to the higher-energy part of the spectrum. On the other hand, the best-fit flux obtained for the high-energy band (panel (b)) does not completely follow (underestimates) the low-energy part of the spectrum. This trend is clearly represented by the normalized residuals, plotted in the respective panels. Panel (d) of Figure 5 shows DEM[T] for the best-fit model photon flux estimated for the input photon spectrum corresponding to the low-, high-, and combined-energy ranges. This enabled us to perform a comparative study of the DEM[T] dependence on the input energy bands selection. We note that the best-fit DEM[T] curves for the low- and high-energy bands yield high peak values of DEM ($\mathrm{DEM_p}$) $= 1.72 \times 10^{49}$ cm^{-3} MK^{-1}; however, at low temperatures, $T_{\rm p} = 7.8$ MK for the former (low-energy band) case and relatively lower $\mathrm{DEM_p} = 1.66 \times 10^{49}$ cm^{-3} MK^{-1} at higher $T_{\rm p} = 8.2$ MK for the latter case. Moreover, moderate $\mathrm{DEM_p}$ at $T_{\rm p}$ best fits the input spectra of the combined energy band.

3.1.2. DEM[T] Distribution Derived from Observed X-Ray Emission During the Flare

We analyze X-ray emission in the low-energy (1.6–5.0 keV) and high-energy (5.0–8.0 keV) bands obtained from SphinX and SOXS, respectively, during the flare. In this regard, we prepare a time series of the spectra by integrating the observed X-ray emission into 120 s time intervals during the periods 04:27–04:33 UT and 04:38–05:00 UT, which correspond to the rise and decay phases of the flare, respectively. On the other hand, better count statistics during the period 04:33–04:38 UT, which correspond to the impulsive phase of the flare, enabled us to integrate the observation in 60 s time intervals. The time sequence of the spectra obtained in such a way serves as the input to the inversion scheme.

We forward fit the observed SXR spectrum in the low-, high-, and combined-energy bands using a model photon flux which is derived using the inversion scheme employing a single Gaussian functional dependence of the DEM on T (see Equation (2)). Panel (a) of Figure 6 presents the observed count rate in the low-energy band (black color) during the period 04:36–04:37 UT, which corresponds to the maximum of the impulsive phase of the flare. Similarly, the X-ray emission in high-energy band (blue color) is analyzed, as shown in panel (b) of the Figure 6, for the aforementioned time interval. Panel (c) presents the analysis of the combined energy band data

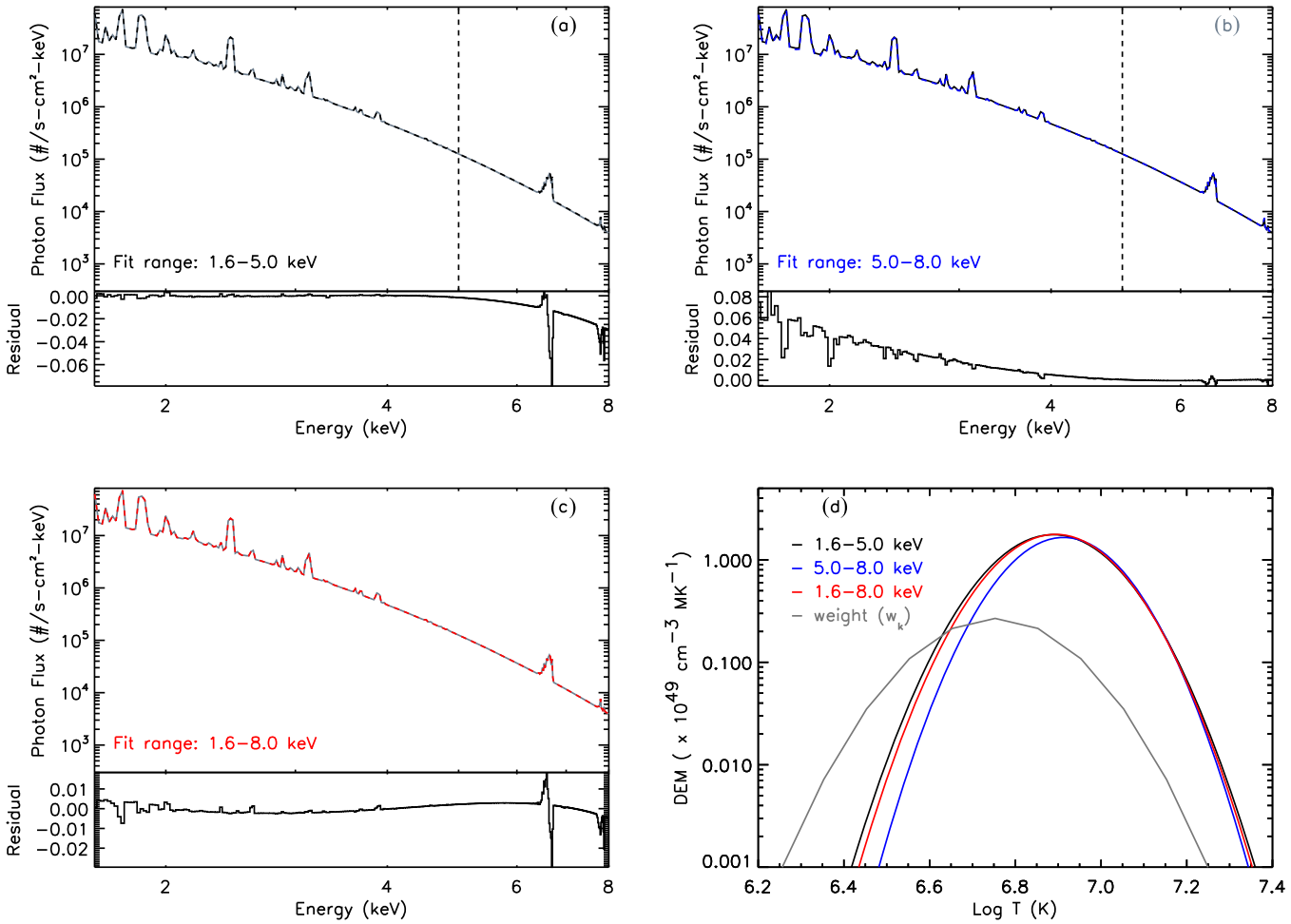

Figure 5. Panels (a), (b), and (c) correspond to the model photon spectrum (gray) overlaid by best-fit model flux for the 1.6–5.0 keV, 5.0–8.0 keV, and 1.6–8.0 keV energy bands, respectively. Normalized residuals are also plotted in the bottom row of all the respective panels. The disagreement of the best-fit curves for the higher and lower parts of the spectrum may be noted. Panel (d) presents the DEM[T] corresponding to the best-fit photon flux for all three energy bands. The normalized weight (w_k), employed in Equation (1), is also shown as a gray plot. The dotted lines in panels (a) and (b) at 5.0 keV represent the boundary of the energy range considered for the spectral fit.

(from SphinX and SOXS) for the time intervals in a manner similar to panels (a) and (b). Best-fit model count rates are over-plotted in red in the respective panels and the derived values are also shown. Panel (d) presents the DEM[T] distribution corresponding to the best-fit model obtained for SXR spectra of the different energy bands.

From Figure 6, it may be noted that the DEM_p estimated from spectral fitting of the low-, high-, and combined-energy band data are 1.40, 0.15, and 0.38 ($\times 10^{49}$cm^{-3} MK^{-1}), respectively. On the other hand, T_p is estimated to be 6.37, 8.93, and 7.57 MK, respectively. It may be noted that the trend of the best-fit parameters, namely, DEM_p and T_p, for three cases of input energy bands is in good agreement with that revealed by the study of model multi-thermal spectrum employing the same inversion scheme as presented in the previous section.

3.2. DEM Varying as a Power-law Function of T

We derive the DEM[T] distribution for the X-ray spectra corresponding to various energy bands, similar to the analysis in the previous section, however, with a different functional dependence of DEM on T. In this multi-thermal model, DEM is approximated to be varying with T in the form of a power law and can be expressed as

$$\mathrm{DEM}(T) \propto \left(\frac{2}{T}\right)^{\gamma}. \quad (3)$$

Next, employing this DEM scheme, we forward fit the observed flare X-ray spectrum in the low-energy band obtained from SphinX (black color) as shown in panel (a) of Figure 7. During the iterative procedure for obtaining the best-fit model, the low-temperature value is fixed to 0.5 keV (5.8 MK), while the maximum temperature is determined as one of the outputs. All of the spectra during the various time intervals of the flare are analyzed, however, here we present only the results from the observations during 04:36–04:37 UT, which are the same as those presented in the previous section. X-ray emission in the high-energy band obtained from SOXS (blue color) is presented in panel (b) of Figure 7. Next, we also fit the observed X-ray spectrum in the combined energy band as shown in panel (c). The best-fit models are over-plotted by red lines in the respective plots. The parameters of the best fit, namely, T_{max}, DEM (at $T = 2$ keV), and the power-law index (γ), are also shown in the respective plots. Panel (d) shows the derived DEM[T] curves corresponding to the best-fit models obtained for different energy ranges.

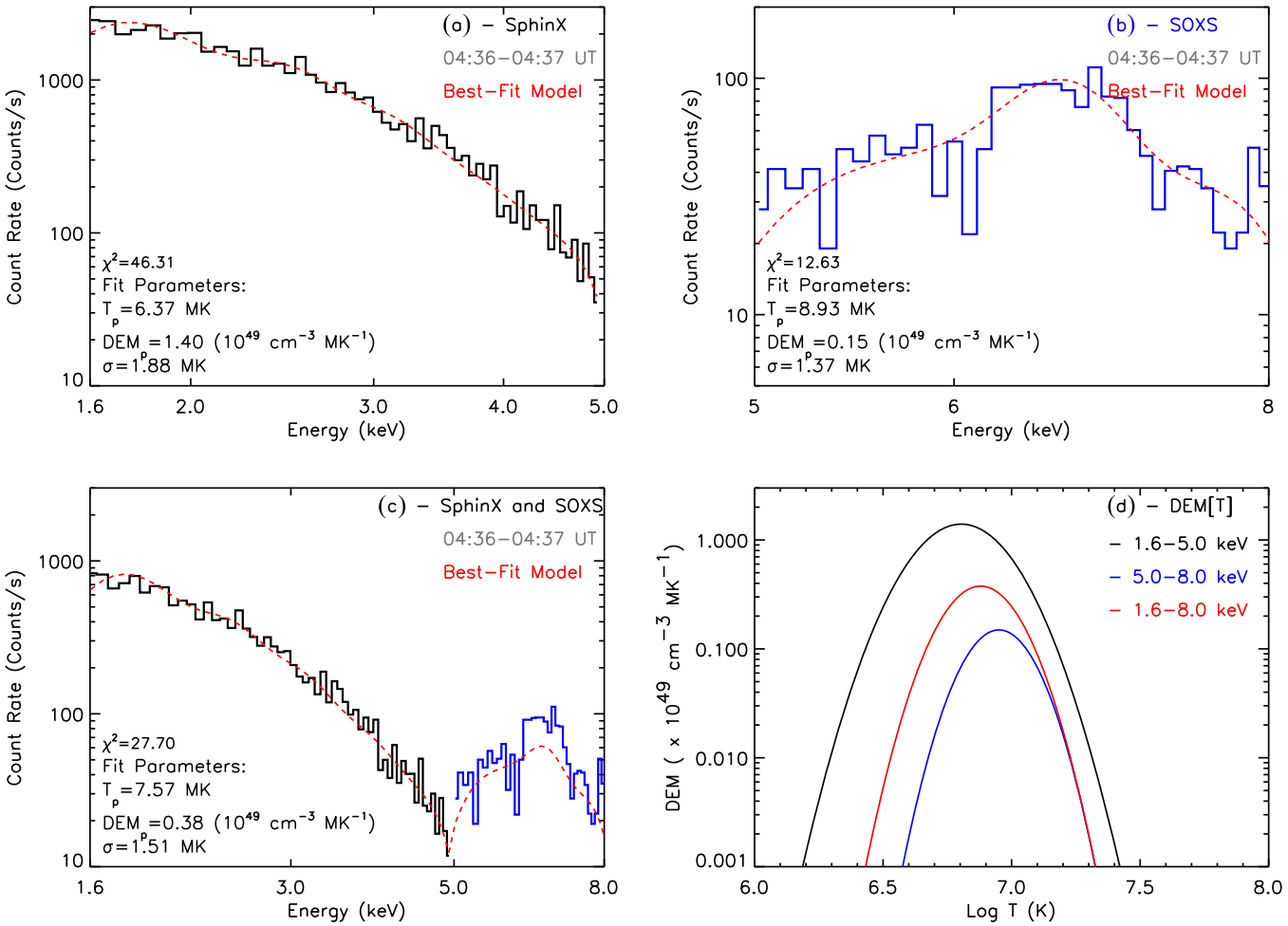

Figure 6. Panels (a), (b), and (c) present the observed spectrum integrated during the maximum phase from SphinX (black) and SOXS (blue) as well as combined data, respectively. Respective best-fit model for the single Gaussian approach is over-plotted in red. Panel (d) presents the derived DEM[T] curves corresponding to the best-fit model for the different energy bands.

In Figure 7, it may be noted that at the peak of the impulsive phase of the flare, the $T_{\max}$ estimated from the observation recorded by SphinX, SOXS, and combined observations is 23.33, 19.58, and 18.47 MK, respectively. It may be noted that the $T_{\max}$ and DEM values estimated in such a way follow the same trend as that which resulted from the previous DEM scheme. Moreover, the negative power-law index (γ) of the best-fit DEM[T] distribution corresponding to the SXR spectrum in the low-, high-, and combined-energy bands is estimated to be 5.46, 4.45, and 4.17, respectively. The less negative (steeper) value of "γ" for the high- and combined-energy cases suggest an enhanced contribution of high-temperature plasma compared to that obtained from the analysis of SXR emission in the low-energy band only.

3.3. W–S Maximum Likelihood DEM Inversion Algorithm

We employ a W–S maximum likelihood DEM inversion algorithm (Sylwester et al. 1980; Kepa et al. 2006, 2008) to the X-ray spectra observed during the flare. The W–S algorithm is a Bayesian numerical technique which employs a maximum likelihood approach in which the DEM distribution in one step of iteration "j" (DEM$_j[T]$) is estimated from that derived in the preceding iteration (DEM$_{j-1}[T]$), and by employing a correction factor (c_i) as well as a weight factor (w_i) in the form given below:

$$\mathrm{DEM}_j[T] = \mathrm{DEM}_{j-1}[T]\frac{\sum_{i=1}^{k} c_i w_i(T)}{\sum_{i=1}^{k}. w_i(T)}. \quad (4)$$

Here, the correction factor, c_i, is estimated from the ratio of the observed flux with the calculated flux, which is derived using the previous DEM distribution form, and can be expressed mathematically as

$$c_i = \frac{F_{\mathrm{obs},i}}{F_{\mathrm{cal},i}}, \quad (5)$$

where $F_{\mathrm{cal},i}$ is the calculated model flux obtained by

$$F_{\mathrm{cal},i} = \int_{j=0}^{\infty} f_i(T)\mathrm{DEM}_j(T)dT. \quad (6)$$

Here, $f_i(T)$ is the theoretical emission function for energy "i" and is derived using the CHIANTI package (Del Zanna et al.

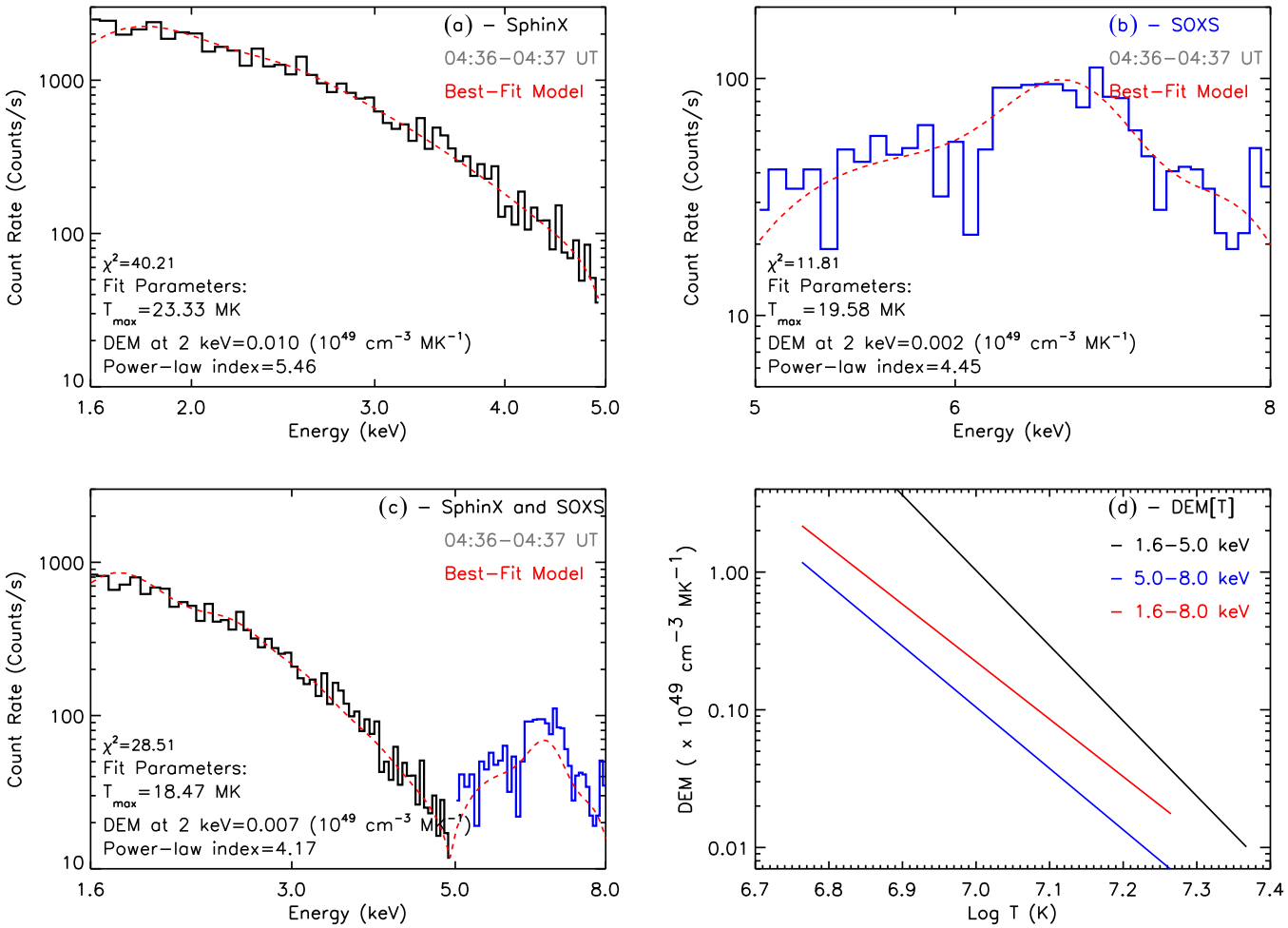

Figure 7. Panels (a) and (b) show the observed count fluxes measured by SphinX (black) and SOXS (blue) during the period 04:36–04:37 UT, respectively. Panel (c) shows the combined X-ray spectra in 1.6–8.0 keV for the time interval, same as in panels (a) and (b). The red curve, over-plotted on the respective panels, represents the best-fit model count flux derived by employing the power-law DEM[T] scheme. Panel (d) presents the derived DEM[T] distribution corresponding to the best-fit model count flux for different energy ranges.

2015). The weight factor w_i is estimated as

$$w_i(T) = f_i(T)\mathrm{DEM}_j(T)dT\frac{\int_{j=0}^{\infty} f_i(T)\mathrm{DEM}_j(T)dT}{\int_{j=0}^{\infty}[f_i(T)\mathrm{DEM}_j(T)]^2 dT} \times \left[\frac{|F_{\mathrm{obs},i} - F_{\mathrm{cal},i}|}{\delta_i} + 1\right]^a. \quad (7)$$

Here, δ_i is the uncertainty corresponding to the observations for energy "i" and "a" is termed as the speed convergence parameter.

We apply the previously noted W–S DEM inversion algorithm to the X-ray spectra obtained from the SphinX and SOXS missions during the flare to obtain the best-fit photon flux and the corresponding DEM[T] distribution. Coronal abundances from the CHIANTI atomic database have been adopted while calculating the theoretical dependence of spectral shapes. The top and middle rows of Figure 8 present the results of the application of the W–S algorithm to the X-ray emission measured by SphinX and SOXS, respectively, during the period 04:27:30–05:00:00 UT, covering the entire flare duration. Moreover, the bottom panel of Figure 8 shows the same, however, here corresponding to the combined data set. The left panel shows the DEM[T] distributions obtained from the best-fit model (red) for the observations, which is shown in the right column.

From the application of the W–S scheme, as shown in Figure 8, we find the peak temperature (T_p) = 10.0, 9.5, and 10.0 MK, and the total EM log(EM) = 47.42, 47.17, and 47.41 (cm^{-3}), corresponding to the SphinX, SOXS and combined energy band data, respectively. This suggests that the trend of the parameters obtained with the W–S scheme for the three cases of the input energy bands is in agreement with that obtained from the previous schemes.

The previously mentiond analysis is made for the spectra obtained by integrating the emission over the whole flare duration. Next, we derive the temporal evolution of the DEM [T] distribution during various phases of the flare by applying the W–S algorithm to the X-ray emission observed during various time intervals of the flare, as presented in Figure 9. The left panels of Figure 9 show the temporal evolution of the best-fit DEM[T] distribution derived over various time intervals of the flare, while the respective right panels show the observed X-ray spectra in the combined energy band (1.6–5.0 and 5.0–8.0 keV, observed by SphinX and SOXS) overlaid by the best-fit model (red).

From Figure 9, it may be noted that the best-fit DEM[T] curve, which is obtained from the analysis of the X-ray

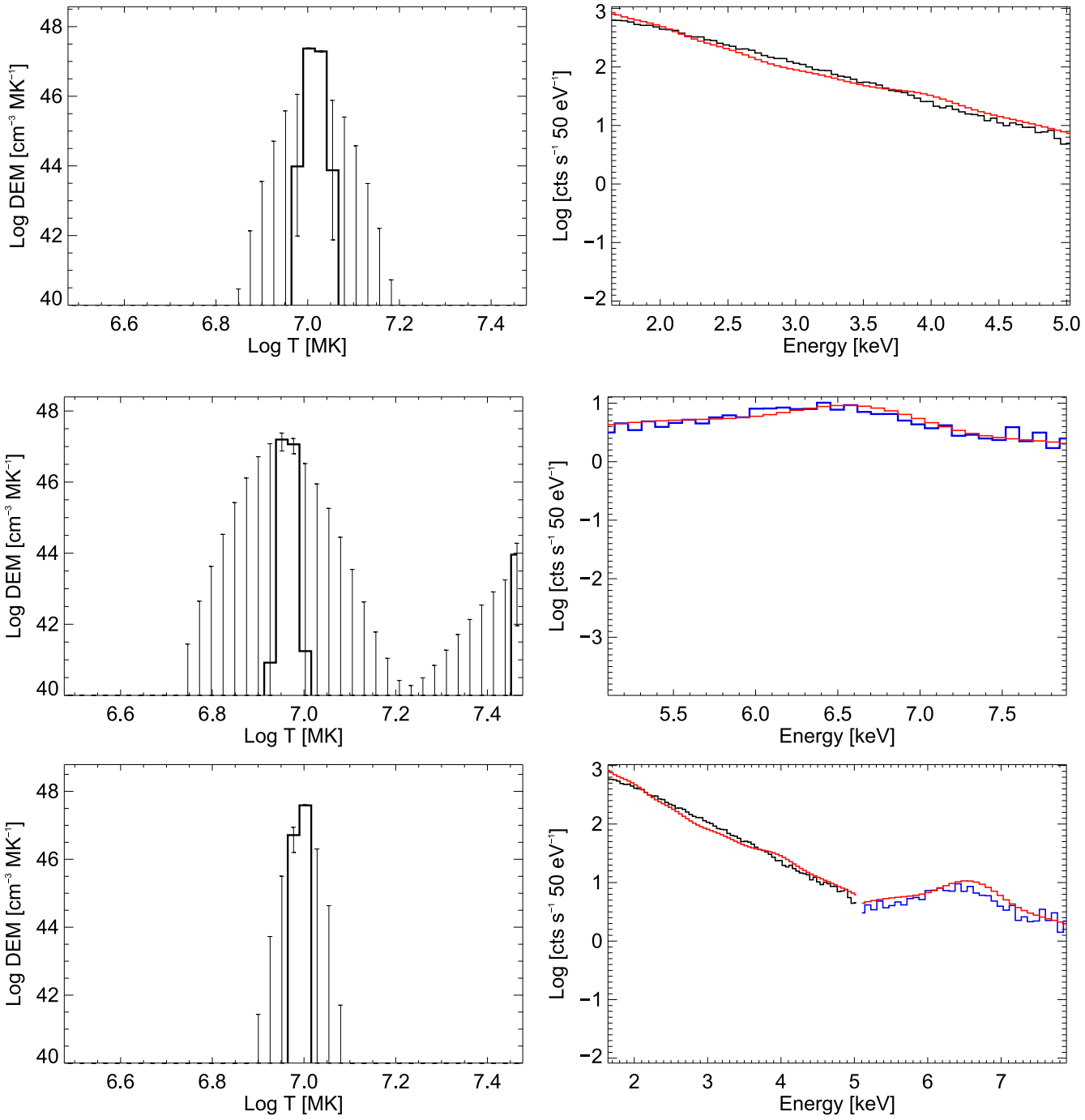

Figure 8. Left column presents the DEM[T] curves related to the best-fit model flux (red), which are derived by employing the W–S procedure to the observed X-ray emission in 1.6–5.0 keV (black) recorded by SphinX (top), 5.0–8.0 keV (blue) obtained from SOXS (middle), and 1.6–8.0 keV from SphinX and SOXS (bottom). The observed X-ray spectrum has been integrated for the time range 04:27:30–05:00:00 UT, which covers the entire flare duration.

emission measured during the flare onset time (04:27:30–04:29:45 UT), can be well approximated by a single Gaussian function of T with a width of ∼1 MK. Moreover, the peak temperature (T_p) is estimated to be 5.62 MK. On the contrary, the best-fit DEM[T] curve obtained by analyzing the spectra during 04:31–04:34 UT, which corresponds to the rise phase of the flare, resembles the double-peak Gaussian with increased widths (in comparison to that during the flare onset) of ∼1.5 MK. Moreover, T_p is estimated to vary in the range of 6.3–14.1 MK. This reveals the signature of the contribution of high-temperature plasma in this phase in addition to the low-temperature component, which was present during the flare onset. Furthermore, the DEM[T] derived for the spectra obtained during 04:32–05:00 UT, corresponding to the peak of the impulsive phase and decay phase of the flare, resulted in a single -peak Gaussian nature, however, with peak temperature varying in the range ∼13.0–5.5 MK.

It is intriguing to note that the best-fit DEM[T] distribution, obtained by integrating the emission in the whole flare duration, as shown in Figure 8, can be well approximated as being isothermal in nature. On the contrary, the temporal evolution of the DEM[T] distribution over various phases of

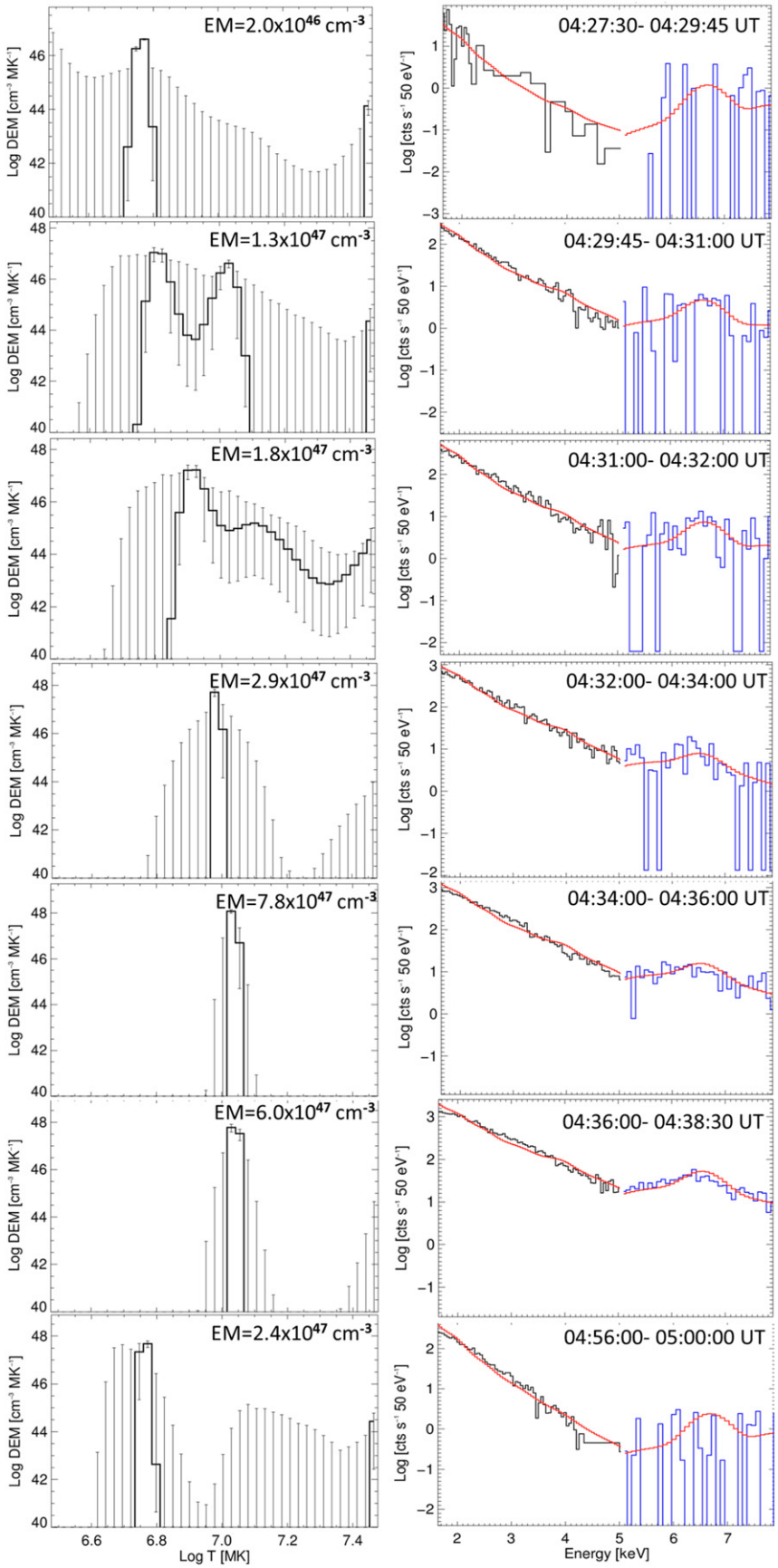

Figure 9. Temporal evolution of best-fit DEM[*T*] distribution (left column) derived using the W–S procedure from the SXR emission (right column) recorded in various phases of the flare. Observed X-ray spectra in 1.6–8.0 keV (1.6–5.0 and 5.0–8.0 keV, observed by SphinX and SOXS are plotted in black and blue, respectively) and the corresponding best-fit model is overlaid in red.

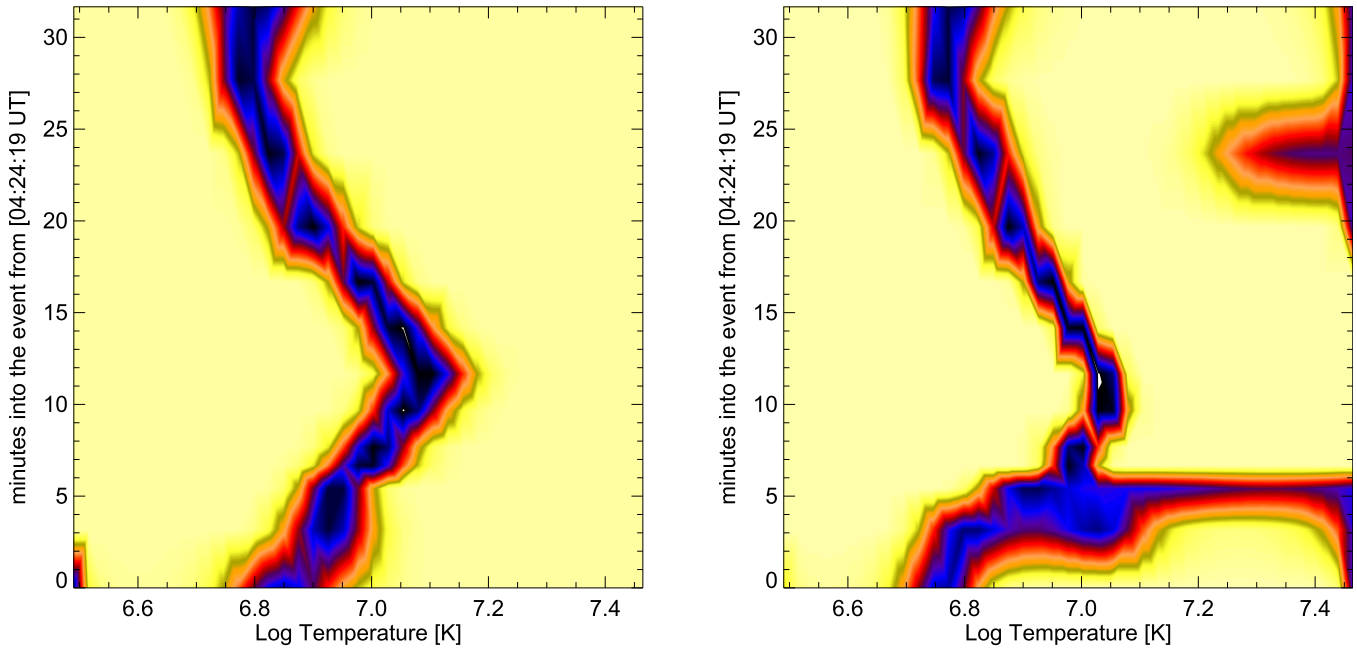

Figure 10. Temporal evolution of the DEM[T] distribution derived from SphinX alone (left) and combined SphinX and SOXS (right) observations.

the flare suggests the presence of multi-thermal plasma during the rise phase of the flare. This apparent inconsistency may be explained by the fact that if the X-ray spectrum is integrated for the whole flare duration, then it is dominated by the emission at the peak of the impulsive phase. Now, it may be noted that the best-fit DEM[T], which is derived for the spectrum during 04:36:00–04:38:30 UT (corresponding to the peak of the impulsive phase, see Figure 9), is isothermal in nature.

In Figure 10, we present a different visualization of the temporal evolution of DEM[T] distribution over the flare duration from the SphinX observations in the left panel while that from the combined-energy band observations is presented in the right panel. The comparison of DEM[T] derived from the SphinX observations alone with that obtained from combined observations reveals a signature of a high-temperature component in the latter analysis during the rise phase of the flare.

4. THERMAL ENERGETICS OF THE FLARE

We estimate the thermal energy content during various phases of the flare. We denote the energy content, which is estimated employing the isothermal approach, as the "isothermal energy," while that derived considering flare plasma, which is of a multi-thermal nature, is termed "multi-thermal energy." Next, we perform a comparative study of the multi-thermal energy content derived by the application of various DEM inversion schemes.

In order to estimate the isothermal energy content of the flare plasma, we derive the temperature (T) and EM by employing the technique presented in Gburek et al. (2013) on the high temporal cadence SphinX spectra. T and EM, derived in such a way, vary in the range of 2.7–15.7 MK and 1.15–28.66 ($\times 10^{47}$ cm^{-3}), respectively. Next, we derive the thermodynamic measure (η; see Sylwester et al. 1995, 2006) which is associated with the thermal energy as follows:

$$E_{\rm th} = 3k_b\eta\sqrt{V}. \quad (8)$$

Here, V is the volume of the emitting plasma. The thermodynamic measure, η, defined as $T\sqrt{\rm EM}$, characterizes the thermal energy of the plasma for the case of the constant volume of the emitting region. In this study, we derive the volume of the emitting region from the EUV images in 284 Å, the hottest channel, as obtained from the *STEREO* twin satellites. Figure 11 shows the sequence of images in 284 Å during the flare recorded by *STEREO*, as well as in 195 Å by EIT/*SOHO*. The contours drawn on the images are 5%, 10%, and 20% of the maximum intensity of the respective images.

From Figure 11, it may be noted that the green contour, corresponding to 20% of the maximum intensity, best represents the emitting region. The volume of the region, assuming spherical geometry, is estimated as follows:

$$V = \frac{4}{3}\pi (R)^3, \quad (9)$$

where "R" is the equivalent radius [$= (A/\pi)^{1/2}$] of a circle having an area (A) equal to that of the region within the isocontour of 20% of the maximum intensity (green) of the images presented in Figure 11. We estimate the temporal evolution of the flare volume from the images in several EUV wavelengths (171, 195, and 284 Å) made available by the *STEREO* and EIT/*SOHO* satellites in the aforesaid manner. However, the volume estimated from the images of 284 Å (representing the hot plasma region) is used to derive the thermal energetics of the flare. As *STEREO* provides the images of the region with a time cadence of 20 minutes, we interpolate the flare volume at intermediate times using a cubic spline interpolation technique. The flare volume, derived in the aforesaid manner, varies in the range 1.2–5.4 ($\times 10^{28}$ cm^3). Using the volume estimated above, we derive the time evolution of the isothermal energy content ($E_{\rm th}$) during the flare using Equation (8) as plotted (black color) in Figure 12. The isothermal energy content estimated in such a way varies

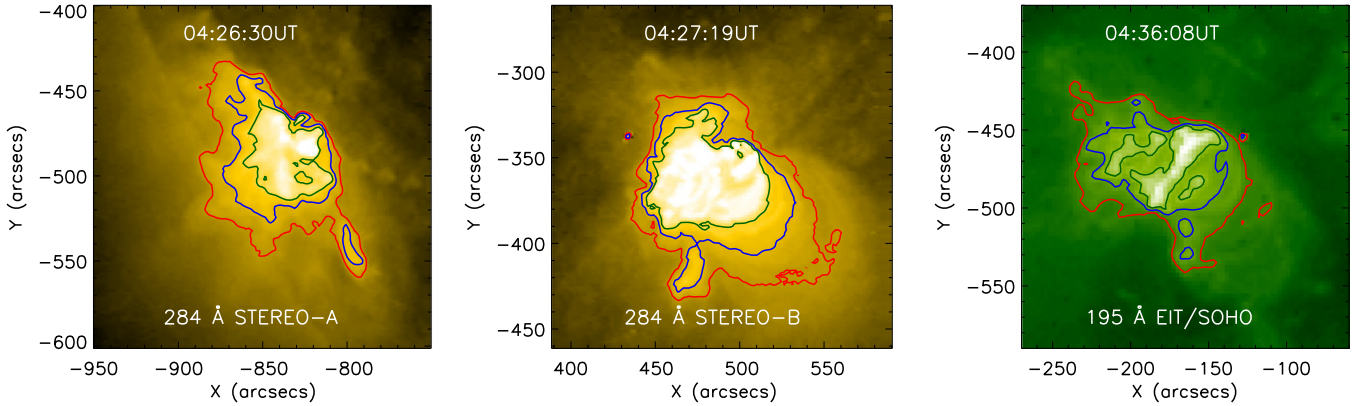

Figure 11. Images in 284 Å during the flare, obtained by *STEREO-A* and *B* as shown in the left and middle panels, respectively. The right panel shows the image obtained during the flare at 195 Å from EIT/*SOHO*. The contours overlaid on the images correspond to 5% (red), 10% (blue), and 20% (green) of the maximum intensity regions.

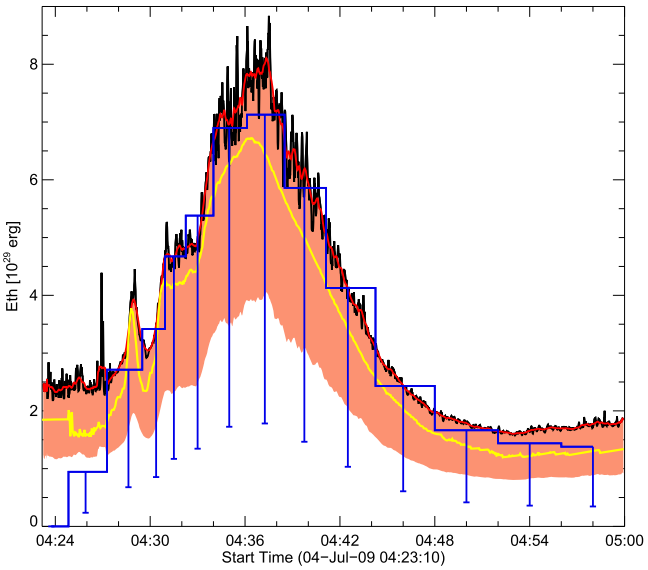

Figure 12. Temporal evolution of the isothermal and multi-thermal energy content during the flare. Isothermal energy, estimated from SphinX observations, is plotted in black (smoothed in red), while that derived from *GOES* observations in shown in yellow. Multi-thermal energy, derived by applying the W–S algorithm to the SphinX and SOXS combined data is shown as the blue histogram. The uncertainty in the estimation of the isothermal energy content is shown by the filled area (light red) while the same corresponding to the multi-thermal energy content is shown in the form of error bars (blue).

in the range (2–9) $\times 10^{29}$ erg. In a similar fashion, we also estimate the isothermal energy content employing the T and EM derived from the *GOES* observations (see Figure 2). Thus the isothermal energy, as derived from the *GOES* observations, is found to vary in the range (1.5–6.5)$\times 10^{29}$ erg during the flare, which is shown by the yellow plot in Figure 12.

The estimate of the source size may contain various kinds of uncertainties, knowledge of which is crucial when investigating as they subsequently propagate to the thermal energy estimates. As the EUV source sizes are used with the DEM[T] distribution (derived from X-ray observations) while estimating the thermal energy content, a disagreement between the cotemporal source sizes within the EUV and X-ray wavebands may become a major contributor to the uncertainty. Unfortunately, imaging mode observations in the X-ray waveband are not available for this flare, and hence EUV images have been used in this study for source size estimation. Although the 284 Å filter provides the peak temperature response (at ∼2 MK), maximum among the other EUV wavelengths available from *STEREO* satellites, it is still quite far from flare plasma temperatures in which X-ray emission is obtained. In this regard, we estimate the co-temporal X-ray and EUV source sizes of 13 flares of intensity class B1.1—C1.0 which occurred during 2009 July 04–06 in active region AR11024. It may be noted that SOL2009-07-04T04:37, the flare considered in our present study, is also produced from the same active region. In this statistical investigation, we have used X-ray images obtained from *HINODE*/XRT and EUV images from the *STEREO* twin satellites in 195 Å. The source size in both the aforementioned wavelengths is estimated by employing the same approach as discussed previously. The comparative investigation has revealed that the source sizes estimated from the X-ray images are systematically smaller than those derived from the EUV images, whereas the ratio varies in the range of 1.1–9.0 with a median value of 6. Next, imaging an asymmetric flaring region with instruments that observe the Sun from different angles, e.g., the observation of AR11024 with the *STEREO-A* and *B* satellites (Figure 3), may contribute to additional uncertainty in the source size estimation. In view of this, we have also made a comparison of the EUV source sizes estimated from 195 Å images obtained from the *STEREO-A* and *B* satellites for our 13 flares. This study revealed that the orthogonal view of the flaring region systematically results in a larger source size by a factor varying in the range of 1.2–1.5 than that calculated from the images with an on-disk view. As the uncertainty in the source size, which arises due to the difference in EUV and X-ray source sizes, is larger than that which occurred due to observing the region from different angles, the latter may be neglected while calculating the uncertainties in the thermal energy estimates. Thus, in conclusion, considering that the EUV source sizes are systematically larger than the X-ray sources by a factor of 6, the volume derived from the same suffers from an overestimate by a factor of 4. Employing the error propagation scheme, the application of the noted uncertainty in the volume estimates may result in an overestimate of the thermal energy content (Equation (9)) by a factor of ∼2. We show the aforementioned uncertainty in the isothermal energy estimate in the form of the associated filled area (light red) in Figure 12.

Next, we estimate the multi-thermal energy content of the flare with the help of the DEM[T] distribution, derived from the W–S inversion scheme, as per the following equation (Sylwester et al. 2014; Aschwanden et al. 2015b):

$$E_{\rm th} = 3k_B V^{1/2} \sum_k T_k {\rm DEM}_k^{1/2}. \quad (10)$$

The multi-thermal energy content derived in such a manner varies in the range of (1–7) $\times$ 10^{29} erg as plotted by the blue histogram in Figure 12. In the estimation of multi-thermal energetics, we have employed the combined data set prepared from the X-ray emission in the 1.6–5.0 keV range as obtained from SphinX, and in the 5.0–8.0 keV range (with the application of a normalization factor of "2.5") from SOXS (see Section 3). It may be argued that this normalization scheme is biased. In this regard, we made a parallel case study in which the best-fit DEM[T] distribution is derived using a combined data set which, however, is prepared by applying the inverse normalization factor to the SphinX observations while considering SOXS observations to be true. This investigation resulted in DEM values which are systematically lower by a factor of 2.5 compared to those estimated in the previous case. On the other hand, the best-fit plasma temperature values remain unchanged (also see Mrozek et al. 2012). Therefore, considering the fact that the DEM values in the former case are larger by the noted factor, i.e., 2.5, the resulting multi-thermal energy content was overestimated by a factor of 4 (Equation (10)). In this calculation, we have also included the uncertainty in the volume estimation obtained previously. In Figure 12, we show the uncertainty in the multi-thermal energy estimates (blue) with the low error bars.

The comparison of the isothermal and multi-thermal energy content for this flare (Figure 12) revealed that multi-thermal energy matches well with the isothermal energy during the rise and decay phases of the flare. However, during the maximum of the impulsive phase, we note minor disagreement in the form of lower values of multi-thermal energy in comparison to the isothermal energy.

Next, we derive the multi-thermal energy from the best-fit DEM[T] distribution, obtained by employing various DEM schemes to the observed SXR spectrum in the 1.6–5.0 keV (low-energy), 5.0–8.0 keV (high-energy), and 1.6–8.0 keV (combined energy) bands during the peak of impulsive phase of the flare (04:36:00–04:38:30 UT). The multi-thermal energy for the low-energy band SXR emission is estimated to be 177, 225, and 4.1 $\times 10^{29}$ erg corresponding to the the single Gaussian, power-law, and W–S DEM schemes, respectively. On the other hand, the energy content derived by employing the aforesaid DEM schemes to the high-energy band SXR is determined to be 64, 65, and 1.5 $\times 10^{29}$ erg, respectively. Furthermore, the multi-thermal energy is 85, 91, and 4.4 $\times 10^{29}$ erg when applying the aforesaid DEM schemes to the combined energy band SXR, respectively. By comparing the above mentioned energy estimates, we note that the flare energetics, estimated from the parameters derived only from the spectral inversion of the low-energy band of the SXR spectrum leads to higher values than that obtained from combined energy band case. On the other hand, the multi-thermal energies, which resulted from applying various DEM schemes to the high-energy part of SXR spectrum, are estimated to be lower than those obtained from combined-energy band SXR spectrum. This trend is consistently noted in the energetics estimated by employing all of the aforementioned DEM schemes. On the contrary, we find that the best-fit DEM[T] distribution, obtained using the DEM schemes which postulate either the single Gaussian or power-law functional dependence of DEM, leads to the overestimation of the multi-thermal energy by approximately one order in comparison to that estimated from W–S algorithm.

5. SUMMARY AND CONCLUSIONS

We investigate the thermal characteristics of the flare plasma by analyzing X-ray emission in the energy band 1.6–8.0 keV observed during the SOL2009-07-04T04:37 flare, which is the only common event observed by both the SphinX and SOXS instruments. We derive the evolution of the best-fit DEM[T] distribution during the flare by employing various DEM inversion algorithms. In addition, we have also studied the dependence of the best-fit DEM[T] corresponding to various input energy bands within the SXR emission. The following are the key points of our study.

1. The best-fit DEM[T] distribution for the low- (1.6–5.0 keV), high- (5.0–8.0 keV), and combined-energy bands (1.6–8.0 keV) of the X-ray emission during the flare resulted in higher values of $\rm DEM_p$, however, at low T_p for the low-energy band in comparison to the relatively lower values of $\rm DEM_p$ at higher T_p obtained by analyzing the high-energy band of the SXR.
2. We derive the time evolution of the DEM[T] distribution during various phases of the flare by employing a W–S maximum likelihood DEM inversion algorithm to individual as well as combined observations from SphinX and SOXS during the flare. The results are summarized as follows.
   a. The best-fit DEM[T] distribution corresponding to the X-ray emission during the flare onset can be well represented by a single Gaussian function with a width of ~1 MK, which suggests the flare plasma to be isothermal in nature during this phase.
   b. Analysis of X-ray emission during the rise to the peak of the impulsive phase of the flare revealed the presence of multi-thermal plasma as the corresponding best-fit DEM[T] curves show a double Gaussian form with widths of ~1.5 MK.
   c. The temporal evolution of the best-fit DEM[T] distribution corresponding to the post-maximum phase of the flare can be well represented by a single Gaussian function, however, with the peak temperature varying in the range ~13.0–5.5 MK.
3. Isothermal and multi-thermal energy content is estimated during the flare. We find that the multi-thermal energy estimates are in close agreement with the isothermal energy values, except during the peak of the impulsive phase of the flare where isothermal energy is estimated to be larger than the multi-thermal energy content.
4. Multi-thermal energy is determined from the best-fit DEM[T] distribution resulting from the application of various inversion schemes to the X-ray emission measured during the peak of the impulsive phase of the flare. We find that the energy content estimated from the parameters derived only from spectral inversion of the low-energy band (1.6–5.0 keV) of the SXR spectrum result in larger values than obtained from the analysis of the SXR emission in combined energy band. On the

contrary, the same derived from only the high-energy band of SXR spectrum leads to lower estimates when comparing with the energy values calculated from combined energy band analysis. This trend is consistently resulted in the thermal energetics determined from all the DEM schemes. This suggests that the observations of SXR emission during a flare in the combined-energy band with high temporal and energy cadence is very important to derive the complete thermal energetics of the flare.

5. The best-fit DEM[T] distribution obtained for the DEM schemes, which postulate either a single Gaussian or power-law functional form of the DEM-T curve, lead to an estimation of the thermal energy content which is much higher, by approximately one order, than that estimated from the W–S scheme. This can be understood by the fact that the width of the best-fit DEM[T] distribution, obtained by employing a single-Gaussian approach (see Figure 6) is larger than that resulting from the application of the W–S scheme (Figure 9). It may be noted that this disagreement between various DEM inversion schemes, and hence thermal energy estimates, can have a significant impact in the context of coronal heating from low-intensity class (micro- and nano-) flares. However, as X-ray emission covers only the high-temperature corona, recent studies focussing coronal heating energized by small intensity flares also combine multi-wavelength observations with the X-ray emission during flares (Testa et al. 2014). Moreover, several advanced schemes of DEM inversion, namely, "DEM_-manual" (Schmelz & Winebarger 2015), "EM Loci approach" (Cirtain et al. 2007), a combination of Gaussian and power-law functional form of DEM (Guennou et al. 2013; Aschwanden et al. 2015a), etc., have also been employed in deriving thermal characteristics of EM during small intensity class flares. Therefore, in the future, we plan to extrapolate the application of the W–S DEM inversion scheme to the combined EUV and X-ray observations during small flares in order to conduct a comparative survey of the thermal energy content derived by the W–S method and other DEM inversion schemes.

This research has been supported by the Polish NCN grant 2011/01/B/ST9/05861 and from the European Commissions Seventh Framework Programme under grant agreement No. 284461 (eHEROES project). Moreover, the research leading to these results has received funding from the European Communitys Seventh Framework Programme (FP7/2007-2013) under grant agreement No. 606862 (F-CHROMA). The authors also acknowledge the open data policy of the SphinX, SOXS, *SOHO*, *HINODE*, and *STEREO* missions. SAO/ADS abstract service is duly acknowledged for providing the up-to-date and well-organized bibliography. Additionally, the Coyote's IDL programming support is acknowledged. The authors also thank the anonymous referee for constructive comments which improved the manuscript.

REFERENCES

Aschwanden, M. J. 2007, ApJ, 661, 1242
Aschwanden, M. J., Boerner, P., Caspi, A., et al. 2015a, SoPh, 290, 2733
Aschwanden, M. J., Boerner, P., Ryan, D., et al. 2015b, ApJ, 802, 53
Aschwanden, M. J., Xu, Y., & Jing, J. 2014, ApJ, 797, 50
Awasthi, A. K., Jain, R., Gadhiya, P. D., et al. 2014, MNRAS, 437, 2249
Benz, A. O. 2008, LRSP, 5, 1
Brown, J. C. 1971, SoPh, 18, 489
Caspi, A., & Lin, R. P. 2010, ApJL, 725, L161
Choudhary, D. P., Gosain, S., Gopalswamy, N., et al. 2013, AdSpR, 52, 1561
Cirtain, J. W., Del Zanna, G., DeLuca, E. E., et al. 2007, ApJ, 655, 598
Craig, I. J. D., & Brown, J. C. 1976, A&A, 49, 239
Dalmasse, K., Chandra, R., Schmieder, B., & Aulanier, G. 2015, A&A, 574, A37
Delaboudinière, J.-P., Artzner, G. E., Brunaud, J., et al. 1995, SoPh, 162, 291
Del Zanna, G., Dere, K. P., Young, P. R., Landi, E., & Mason, H. E. 2015, A&A, 582, A56
Dere, K. P., & Cook, J. W. 1979, ApJ, 229, 772
Fletcher, L., Dennis, B. R., Hudson, H. S., et al. 2011, SSRv, 159, 19
Gburek, S., Sylwester, J., Kowalinski, M., et al. 2011, SoSyR, 45, 189
Gburek, S., Sylwester, J., Kowalinski, M., et al. 2013, SoPh, 283, 631
Guennou, C., Auchère, F., Klimchuk, J. A., Bocchialini, K., & Parenti, S. 2013, ApJ, 774, 31
Jain, R., Aggarwal, M., & Sharma, R. 2008, JApA, 29, 125
Jain, R., Awasthi, A. K., Chandel, B., et al. 2011a, SoPh, 271, 57
Jain, R., Awasthi, A. K., Rajpurohit, A. S., & Aschwanden, M. J. 2011b, SoPh, 270, 137
Jain, R., Dave, H., Shah, A. B., et al. 2005, SoPh, 227, 89
Kepa, A., Sylwester, B., Siarkowski, M., & Sylwester, J. 2008, AdSpR, 42, 828
Kepa, A., Sylwester, J., Sylwester, B., Siarkowski, M., & Stepanov, A. I. 2006, SoSyR, 40, 294
Kulinová, A., Kašparová, J., Dzifčáková, E., et al. 2011, A&A, 533, A81
Landi, E., Del Zanna, G., Young, P. R., Dere, K. P., & Mason, H. E. 2012, ApJ, 744, 99
Li, H., Berlicki, A., & Schmieder, B. 2005, A&A, 438, 325
Mrozek, T., Gburek, S., Siarkowski, M., et al. 2012, CEAB, 36, 71
Saint-Hilaire, P., & Benz, A. O. 2005, A&A, 435, 743
Schmelz, J. T., & Winebarger, A. R. 2015, RSPTA, 373, 20140257
Shibata, K. 1999, Ap&SS, 264, 129
Sylwester, B., Sylwester, J., Kepa, A., et al. 2006, SoSyR, 40, 125
Sylwester, B., Sylwester, J., Phillips, K. J. H., Kępa, A., & Mrozek, T. 2014, ApJ, 787, 122
Sylwester, J., Garcia, H. A., & Sylwester, B. 1995, A&A, 293, 577
Sylwester, J., Kowalinski, M., Gburek, S., et al. 2012, ApJ, 751, 111
Sylwester, J., Schrijver, J., & Mewe, R. 1980, SoPh, 67, 285
Testa, P., De Pontieu, B., Allred, J., et al. 2014, Sci, 346, 1255724